

We are IntechOpen, the world's leading publisher of Open Access books Built by scientists, for scientists

6,900

Open access books available

186,000

International authors and editors

200M

Downloads

Our authors are among the

154

Countries delivered to

TOP 1%

most cited scientists

12.2%

Contributors from top 500 universities



WEB OF SCIENCE™

Selection of our books indexed in the Book Citation Index
in Web of Science™ Core Collection (BKCI)

Interested in publishing with us?
Contact book.department@intechopen.com

Numbers displayed above are based on latest data collected.
For more information visit www.intechopen.com



Thermal Stability and Phase Transformations of Multicomponent Iron-Based Amorphous Alloys

Milica M. Vasić, Dušan M. Minić and Dragica M. Minić

Abstract

Due to their excellent functional properties enabling their applicability in different fields of modern technology, amorphous alloys (metallic glasses) based on iron have been attracting attention of many scientists. In this chapter, the results of multidisciplinary research of five multicomponent iron-based amorphous alloys with different chemical composition, $\text{Fe}_{81}\text{Si}_4\text{B}_{13}\text{C}_2$, $\text{Fe}_{79.8}\text{Ni}_{1.5}\text{Si}_{5.2}\text{B}_{13}\text{C}_{0.5}$, $\text{Fe}_{75}\text{Ni}_2\text{Si}_8\text{B}_{13}\text{C}_2$, $\text{Fe}_{73.5}\text{Cu}_1\text{Nb}_3\text{Si}_{15.5}\text{B}_7$, and $\text{Fe}_{40}\text{Ni}_{40}\text{P}_{14}\text{B}_6$, are summarized in order to study the influence of chemical composition on their physicochemical properties and functionality. The research involved thermal stability, mechanism, thermodynamics, and kinetics of microstructural transformations induced by thermal treatment and their influence on functional properties. Determination of crystallization kinetic triplets of individual phases formed in the alloys is also included. The results obtained for different alloys are compared, correlated, and discussed in terms of the alloy composition and microstructure.

Keywords: amorphous alloys, iron, microstructure, crystallization, kinetics, functional properties

1. Introduction

Amorphous alloys (metallic glasses), composed of metallic and metalloid elements, characterized by a short-range atomic ordering, have been attracting a lot of scientific attention because of their extraordinary isotropic physical and mechanical properties [1–3]. Within this class of materials, the iron-based alloys stand out by a unique combination of magnetic, electrical, mechanical, and anticorrosion properties, which makes them suitable for many applications, as multifunctional materials [3–5]. Their applications as soft magnetic materials are mainly based on their low coercivity, high permeability, high saturation induction, low eddy current losses, low magnetic reversal losses, and high Curie temperature [6, 7]. Due to their high strength and hardness, large elastic elongation limit, and good corrosion resistance, amorphous alloys are convenient for different structural applications [3, 8]. Their functional properties as well as their thermal stability can be tuned by an appropriate choice of alloying elements. It is considered that the glass-forming ability of the alloy is improved if empirical component rules [9, 10] are fulfilled:

alloy should include more than three elements, metallic and nonmetallic, in the composition where the differences in atomic size of the three constituent elements are higher than 12%, negative heats of mixing among the main three constituents, a total amount of nonmetallic components of around 20 atomic %, and the absence of oxide inclusions. The alloys composed of more elements exhibit better glass-forming ability, which is known as “confusion principle” [11].

Thermodynamic metastability and kinetic metastability are among the key characteristics of amorphous alloys in general. Consequently, there is a high tendency for their transformations to more stable forms to occur under the conditions of elevated temperature and pressure or even during prolonged usage at moderate temperatures. These transformations include structural relaxation, glass transition, crystallization, and recrystallization processes, which affect the functional properties of the alloys, involving either their deterioration or improvement [12, 13]. When nanocrystals are formed in an amorphous matrix making a composite, the properties of the material are determined by crystal dimensions and volume fraction of the present nanocrystals. In the case of iron-based materials, the best hard magnetic properties can be obtained for full or almost full crystallization of the starting amorphous material, while the optimal soft magnetic properties can be achieved in the case of partial crystallization [14]. Accordingly, in order to tailor materials with targeted functional properties, information about thermal stability as well as the knowledge of mechanism and kinetics of thermally induced structural changes and their influence on functional properties of these materials are very important.

The goal of this chapter is to correlate and explain the results of our multidisciplinary studies [15–30] of five multicomponent iron-based amorphous alloys of different compositions, $\text{Fe}_{81}\text{Si}_4\text{B}_{13}\text{C}_2$, $\text{Fe}_{79.8}\text{Ni}_{1.5}\text{Si}_{5.2}\text{B}_{13}\text{C}_{0.5}$, $\text{Fe}_{75}\text{Ni}_2\text{Si}_8\text{B}_{13}\text{C}_2$, $\text{Fe}_{73.5}\text{Cu}_1\text{Nb}_3\text{Si}_{15.5}\text{B}_7$, and $\text{Fe}_{40}\text{Ni}_{40}\text{P}_{14}\text{B}_6$, in terms of mechanism, thermodynamics, and kinetics of thermally induced microstructural transformations.

2. Experimental

Iron-based amorphous alloys studied herein were prepared in the form of the 30–35 μm thin ribbons by melt-quenching technique [15–30]. The nominal composition of the as-prepared alloy samples can be represented as follows in atomic %: $\text{Fe}_{81}\text{Si}_4\text{B}_{13}\text{C}_2$, $\text{Fe}_{79.8}\text{Ni}_{1.5}\text{Si}_{5.2}\text{B}_{13}\text{C}_{0.5}$, $\text{Fe}_{75}\text{Ni}_2\text{Si}_8\text{B}_{13}\text{C}_2$, $\text{Fe}_{73.5}\text{Cu}_1\text{Nb}_3\text{Si}_{15.5}\text{B}_7$, and $\text{Fe}_{40}\text{Ni}_{40}\text{P}_{14}\text{B}_6$.

X-ray diffraction (XRD) measurements were performed in Bragg-Brentano geometry, using a Co K_α radiation source, at room temperature. Preparation of thermally treated samples included isothermal annealing of the alloy samples sealed in a quartz ampoule at selected temperatures, for 60 min in the case of the $\text{Fe}_{79.8}\text{Ni}_{1.5}\text{Si}_{5.2}\text{B}_{13}\text{C}_{0.5}$ alloy and for 30 min for all the other alloys. Qualitative and quantitative analyses of the collected XRD data of the as-prepared and thermally treated samples were conducted using ICSD [31], PDF-2 [32], and COD [33] databases and Maud [34] software.

Transmission electron microscopy (TEM) images were recorded with a Philips CM12 microscope (tungsten cathode, 120 kV electron beam). For TEM measurements, samples were prepared using the focused-ion beam (FIB) method (Ga ions). JEOL JSM 6460 was used to collect scanning electron microscopy (SEM) images.

Thermal analyses of the studied alloys were carried out by means of differential scanning calorimetry (DSC) in a protective nitrogen or helium atmosphere, at constant heating rates. Complex crystallization peaks were deconvoluted [19, 21–24]

using either Gaussian-Lorentzian cross-product function or Fraser-Suzuki function, taking into consideration the criteria related to the nature of the process as well as the mathematical criteria.

Thermomagnetic measurements were conducted in an evacuated furnace using an EG&G vibrating sample magnetometer, under magnetic field of 4 kA m^{-1} , at constant heating rate. Electrical resistivity measurements were performed by the four-point method, in an inert atmosphere. Vickers microhardness was determined using MHT-10 (Anton Paar, Austria) microhardness testing device, with 0.4 N loads and 10 s loading time.

3. Results and discussion

Considering the metastability of amorphous alloys, preservation of microstructure and knowledge of thermal stability in wide temperature range are crucial for their practical applications. In this sense, our investigations start by structural characterization of several as-prepared Fe-based amorphous alloys of different chemical compositions, followed by thermal analysis.

3.1 Structural characterization of the as-prepared alloys

In order to obtain detailed information on microstructure of the as-prepared alloys and the nature of individual crystallization steps, the XRD and Mössbauer spectroscopy methods were applied [15, 20, 25, 28, 30]. The XRD results revealed that the microstructure of the as-prepared alloys is characterized by short-range atomic ordering showing characteristic broad diffraction halo maxima. According to the positions of broad diffraction halo maxima ($2\theta = 52$ and 96° , **Figure 1**), the starting atomic configuration corresponds to the bcc-Fe structure, for all the studied alloys. Short-range ordering domain sizes for all the alloys were estimated to be approximately 1.6 nm according to the Scherrer equation [35].

Nevertheless, the as-prepared structures of the $\text{Fe}_{73.5}\text{Cu}_1\text{Nb}_3\text{Si}_{15.5}\text{B}_7$ and $\text{Fe}_{81}\text{B}_{13}\text{Si}_4\text{C}_2$ alloys are not completely amorphous, containing certain amounts of crystalline phases. Based on the sharp maximum in the XRD diagram (**Figure 1**) and the results of Mössbauer spectroscopy [28], 5% of the structure of the

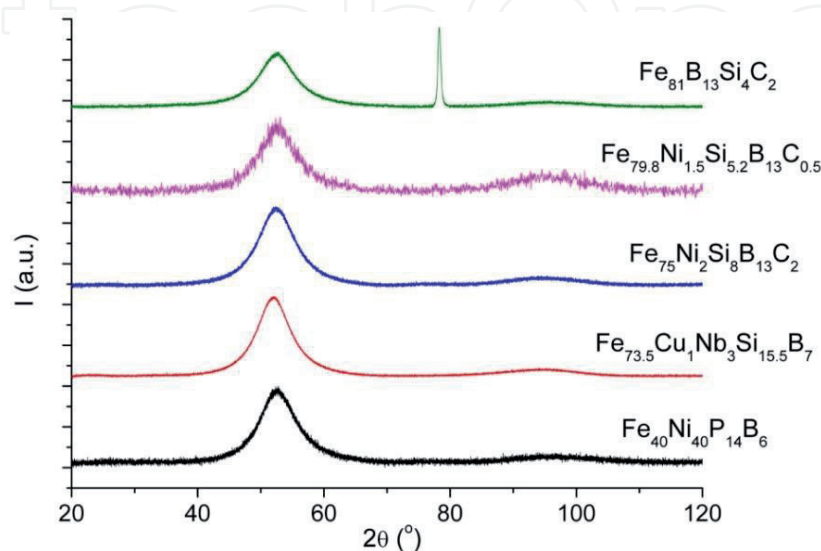


Figure 1.
XRD patterns of the as-prepared alloys.

as-prepared $\text{Fe}_{81}\text{B}_{13}\text{Si}_4\text{C}_2$ alloy is in crystalline form. This can be caused by high Fe content in this alloy and the fact that it does not contain any metal element other than Fe, so the requirements for easier amorphization [11] are not fully met. On the other hand, according to Mössbauer spectroscopy [20], 3.5% of the structure of the as-prepared $\text{Fe}_{73.5}\text{Cu}_1\text{Nb}_3\text{Si}_{15.5}\text{B}_7$ alloy correspond to crystalline clusters and disappear on heating, during the process of structural relaxation. This amount of crystalline phase is very close to the lowest amount which could be detected by XRD and consequently was not noticed in the XRD patterns (**Figure 1**). The appearance of crystallinity in this case was contributed by the presence of Cu atoms, which, when present in small amounts, form clusters serving as precursors for nucleation of the α -Fe(Si) crystalline phase.

3.2 Thermal stability of the alloys

According to the results of thermal analysis, all of the studied alloys possess good thermal stability at temperature under 380°C (**Figure 2a**). The glass transition preceding crystallization can be clearly observed only for the $\text{Fe}_{79.8}\text{Ni}_{1.5}\text{Si}_{5.2}\text{B}_{13}\text{C}_{0.5}$ and $\text{Fe}_{81}\text{B}_{13}\text{Si}_4\text{C}_2$ alloys (**Figure 2b**), suggesting their higher glass-forming ability than those of the other alloys studied. By applying DSC method, correlation between thermal stability of the alloys and their chemical composition was observed. The lowest thermal stability was demonstrated by the alloy with lower content of iron, $\text{Fe}_{40}\text{Ni}_{40}\text{P}_{14}\text{B}_6$, containing P instead of Si, with the beginning of crystallization at round 380°C . The alloys with higher content of iron show higher thermal stability, where the alloys $\text{Fe}_{73.5}\text{Cu}_1\text{Nb}_3\text{Si}_{15.5}\text{B}_7$, $\text{Fe}_{75}\text{Ni}_2\text{Si}_8\text{B}_{13}\text{C}_2$, and $\text{Fe}_{81}\text{B}_{13}\text{Si}_4\text{C}_2$ begin to crystallize at around 500°C and $\text{Fe}_{79.8}\text{Ni}_{1.5}\text{Si}_{5.2}\text{B}_{13}\text{C}_{0.5}$ even at around 520°C . The temperatures corresponding to the start of crystallization observed for the examined alloys (**Table 1**) are in agreement with the literature data for the similar systems [36]. A somewhat higher thermal stability of the $\text{Fe}_{79.8}\text{Ni}_{1.5}\text{Si}_{5.2}\text{B}_{13}\text{C}_{0.5}$ alloy was also suggested by a wide temperature range corresponding to supercooled liquid region (**Figure 2b**). This behavior results from the optimal chemical composition including two metal elements with the total content of around 80% (at.) and three nonmetallic amorphizers with the total content of around 20%.

The peak shape of exothermal stabilization maxima, sharp or rounded in some degree, and the presence of more than one maximum (**Figure 2**) indicate the occurrence of several parallel or consecutive steps of thermal stabilization, for all the studied alloys [19, 21–24]. The alloys containing higher amount of iron ($\text{Fe}_{79.8}\text{Ni}_{1.5}\text{Si}_{5.2}\text{B}_{13}\text{C}_{0.5}$ and $\text{Fe}_{81}\text{B}_{13}\text{Si}_4\text{C}_2$) exhibit one well-defined sharp crystallization peak, while the alloys with slightly lower amount of iron ($\text{Fe}_{73.5}\text{Cu}_1\text{Nb}_3\text{Si}_{15.5}\text{B}_7$ and $\text{Fe}_{75}\text{Ni}_2\text{Si}_8\text{B}_{13}\text{C}_2$) show two distinct completely separated compounded peaks (**Figure 2a**), which correspond to different crystallization and recrystallization steps. The alloy containing equal amounts of Fe and Ni (40% at.) exhibits two (one compounded and one sharp) partially overlapped DSC peaks, pointing out several crystallization steps.

The enthalpies of different crystallization steps for all the alloys are determined from the area corresponding to DSC peaks at various heating rates. Various heating rates yield different enthalpy values, showing that thermal history of a sample has a significant impact on the final state of the system. The starting state of the system is the same, but the final state is influenced by duration of thermal treatment as well as by the temperature, influencing the value of determined enthalpies. The observed average absolute values of the enthalpies at heating rates $5\text{--}20^\circ\text{C min}^{-1}$ (**Table 1**) for crystallization are $80\text{--}110\text{ J/g}$, but for recrystallization are around 20 J/g .

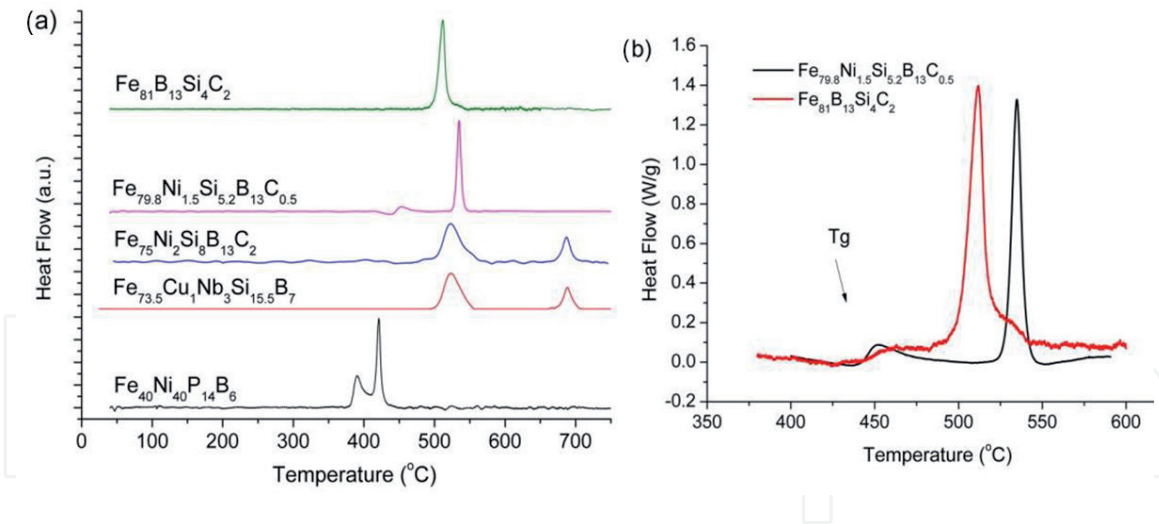


Figure 2. DSC curves of the studied alloys at 5°C/min (a) and corresponding curves of the $Fe_{79.8}Ni_{1.5}Si_{5.2}B_{13}C_{0.5}$ and $Fe_{81}B_{13}Si_4C_2$ alloys in the temperature region 380–600°C indicating glass transition, T_g (b).

		T_0 (°C)	$ \Delta H $ (J g ⁻¹)	T_{c1} (°C)	T_{c2} (°C)
$Fe_{81}B_{13}Si_4C_2$	α -Fe(Si), Fe_3B , Fe_2B	500	87	420	730
$Fe_{79.8}Ni_{1.5}Si_{5.2}B_{13}C_{0.5}$	α -Fe(Si), Fe_2B	520	110 ± 10	—	—
$Fe_{75}Ni_2Si_8B_{13}C_2$	Peak 1 α -Fe(Si), Fe_3B , Fe_2B	500	80 ± 20	430	740
	Peak 2	670	20 ± 6		
$Fe_{73.5}Cu_1Nb_3Si_{15.5}B_7$	Peak 1 α -Fe(Si), Fe_2B	500	90 ± 20	340	600
	Peak 2 $Fe_{16}Nb_6Si_7$, Fe_2Si	670	20 ± 10		
$Fe_{40}Ni_{40}P_{14}B_6$	α -(Fe,Ni), γ -(Fe,Ni), (Fe,Ni) ₃ (P,B)	380	—	360	480

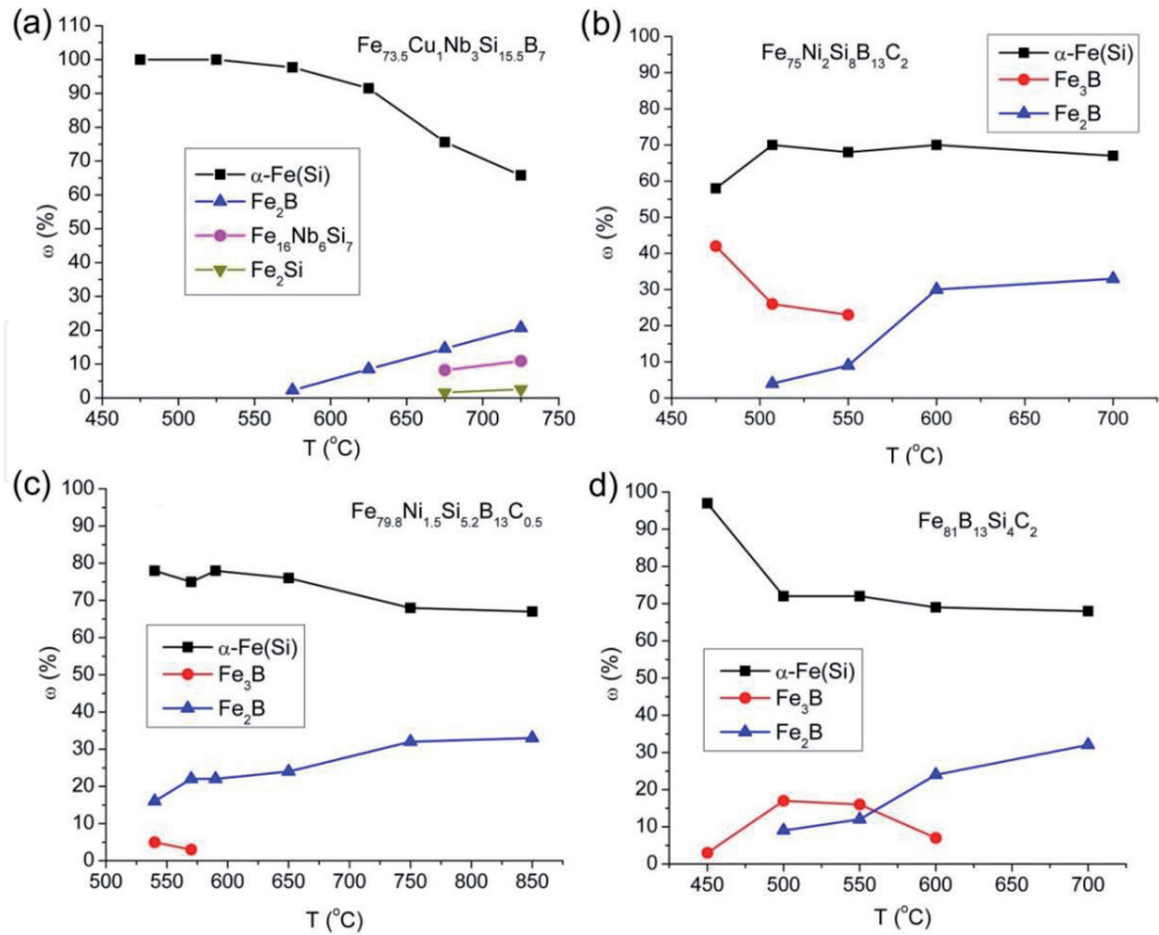
Table 1. Temperatures of the crystallization onset (T_c), average absolute values of the transformation enthalpies ($|\Delta H|$), and Curie temperatures (T_c), for individual amorphous alloys.

3.3 Thermally induced structural transformations

For more information on thermally induced microstructural transformation of the alloys and the nature of individual crystallization steps, the XRD, Mössbauer spectroscopy, and SEM and TEM methods were applied on the alloy samples isothermally treated at different temperatures, chosen according to the DSC thermograms.

With thermal treatment of the alloys, new narrow peaks appear in the XRD diffractograms as a result of crystallization. The changes of their relative intensities and areas point out the changes in microstructural parameters of the formed phases provoked by thermal treatment at different temperatures. The appearance and disappearance of some sharp peaks in the XRD patterns with a rise in temperature of thermal treatment indicate the processes of recrystallization and formation of one phase at the expense of another [15, 18, 20, 26, 30]. The analysis of the obtained XRD patterns yielded the information about microstructure of the studied samples and the phase composition diagrams (Figure 3, Table 2).

Due to the presence of bcc-Fe-like atomic configuration in the ordered domains of the as-prepared alloys, the α -Fe(Si) phase is the first crystalline phase formed in amorphous matrix during thermal treatment of the alloys [15, 18, 20, 26, 30].


Figure 3.

Phase composition diagrams of the alloys containing 73–81 atomic % of iron ($Fe_{73.5}Cu_1Nb_3Si_{15.5}B_7$ (a), $Fe_{75}Ni_2Si_8B_{13}C_2$ (b), $Fe_{79.8}Ni_{1.5}Si_{5.2}B_{13}C_{0.5}$ (c), $Fe_{81}B_{13}Si_4C_2$ (d)), showing the fractions of individual phases relative to the total amount of the crystalline material in the alloy ((a) is reprinted from ref. [16] with permission of Institute of Physics of Polish Academy of Sciences).

Annealing temperature (°C)	Phases
340	α -(Fe,Ni); γ -(Fe,Ni)
370	α -(Fe,Ni); γ -(Fe,Ni); $(Fe,Ni)_3(P,B)$
400	α -(Fe,Ni); γ -(Fe,Ni); $(Fe,Ni)_3(P,B)$
420	α -(Fe,Ni); γ -(Fe,Ni); $(Fe,Ni)_3(P,B)$
500	γ -(Fe,Ni); $(Fe,Ni)_3(P,B)$
600	γ -(Fe,Ni); $(Fe,Ni)_3(P,B)$

Table 2.

Crystalline phases present in the $Fe_{40}Ni_{40}P_{14}B_6$ alloy after thermal treatment at different temperatures.

For these alloys, the beginning of crystallization of the α -Fe(Si) phase from the amorphous structure is observed at approximately the same temperatures (around 450–500°C), with the exception of the $Fe_{40}Ni_{40}P_{14}B_6$ alloy containing the lowest amount of iron (380°C). This phase remains the dominant crystalline phase over the whole temperature range examined. Formation of the α -Fe(Si) phase is also contributed by a tendency toward creation of stronger bonds between Fe and Si than between Fe and B, and repulsion between Si and B, as indicated by ab initio molecular dynamic simulations [37].

Crystallization of the α -Fe(Si) phase brings about favorable conditions for crystallization of boride phases, since in amorphous matrix, in the vicinity of

α -Fe(Si) grains, the ratio of boron to iron concentration is increased. This is contributed by several factors. Formation of α -Fe(Si) crystalline grains reduces Fe content in the amorphous matrix, while the boron is repulsed out of the α -Fe(Si) crystalline grains because of its low solubility in α -Fe and the presence of Si in this crystalline phase. Thus, amorphous/crystal interphase boundaries, being boron enriched, serve as nucleation sites for crystallization of boron phases. In the alloys containing 13 atomic % of boron ($\text{Fe}_{81}\text{B}_{13}\text{Si}_4\text{C}_2$, $\text{Fe}_{79.8}\text{Ni}_{1.5}\text{Si}_{5.2}\text{B}_{13}\text{C}_{0.5}$, and $\text{Fe}_{75}\text{Ni}_2\text{Si}_8\text{B}_{13}\text{C}_2$), two boride crystalline phases appear during heating: metastable Fe_3B and stable Fe_2B . In the case of $\text{Fe}_{73.5}\text{Cu}_1\text{Nb}_3\text{Si}_{15.5}\text{B}_7$, which contains 7 atomic % of boron, the metastable Fe_3B phase is observed only using Mössbauer spectroscopy and in lower amount than in the alloys containing higher quantity of boron [20]. Upon further heating, the metastable Fe_3B phase is transformed into the stable Fe_2B phase. The highest content of the Fe_3B phase is observed in the $\text{Fe}_{75}\text{Ni}_2\text{Si}_8\text{B}_{13}\text{C}_2$ alloy (**Figure 3**), which could be a consequence of the presence of a suitable amount of Ni in the alloy, since it is considered that the Ni element present in an appropriate amount can retard the degradation of metastable boride phases [38]. In the case of the $\text{Fe}_{79.8}\text{Ni}_{1.5}\text{Si}_{5.2}\text{B}_{13}\text{C}_{0.5}$ alloy, the Fe_3B phase can be observed only in very low amounts (few wt. % of crystalline phases) (**Figure 3c**), which is partially caused by longer heating time during sample preparation (60 min instead of 30 min). For all the alloys with Fe as the dominant component, crystalline phases α -Fe(Si) and Fe_2B are observed as final crystallization products [15, 16, 25, 28]. For the alloys containing 13 atomic % of boron, at the highest temperatures of thermal treatment, weight percentages of the α -Fe(Si) and Fe_2B crystalline phases are 70 and 30%, respectively, while, in the case of the $\text{Fe}_{73.5}\text{Cu}_1\text{Nb}_3\text{Si}_{15.5}\text{B}_7$ alloy, weight percentage of the Fe_2B phase at the highest temperatures of thermal treatment is lower (around 20% wt.), due to the lower boron content in the alloy. In addition, in this alloy, crystalline phases $\text{Fe}_{16}\text{Nb}_6\text{Si}_7$ and Fe_2Si are formed after heating at high temperatures [16], because of higher Si content than in the other alloys examined and the presence of Nb. Similarly to the alloys with Fe as the dominant component, crystallization of the $\text{Fe}_{40}\text{Ni}_{40}\text{P}_{14}\text{B}_6$ alloy starts with the formation of the bcc-structured phase, α -(Fe,Ni), but in this case it starts at lower annealing temperatures, 340–380°C. However, the crystallization mechanisms of the $\text{Fe}_{40}\text{Ni}_{40}\text{P}_{14}\text{B}_6$ alloy are somewhat different from those of the alloys containing 73–81% Fe and include the formation of crystalline phases α -(Fe,Ni), γ -(Fe,Ni), and $(\text{Fe,Ni})_3(\text{P,B})$ and transformation of the α -(Fe,Ni) phase into γ -(Fe,Ni) and $(\text{Fe,Ni})_3(\text{P,B})$ at high temperatures [18]. Actually, at higher temperatures, the crystalline phase with body centered cubic structure (α -(Fe,Ni)) is destabilized by high Ni content.

Application of TEM method confirms the results of XRD analysis and Mössbauer spectroscopy in terms of crystalline phases formed during heating [18, 20], showing that, after heating at the highest temperatures, the alloy structure is composed of grains, several 10s to several 100s of nanometers in size and irregular in shape, which are formed by coalescence of neighboring grains and influenced by impingement (**Figure 4**) [19–21]. Crystallization changes the morphology of the alloy sample and the distribution of individual elements on the surface of a sample [19, 20], which, after formation of crystalline phases, becomes nonuniform. As a result of crystallization, the alloy structure is more porous, because of imperfect packing of the crystals (**Figure 4b**) [17, 20, 26]. Surface morphology depends significantly on the heating rate and the temperature up to which the sample was heated, in other words on thermal history of a sample [19].

The thermal treatment causes continuous growth of the average crystallite size of α -Fe(Si) and Fe_2B phases in the alloys containing Fe as the dominant metal component except for the $\text{Fe}_{73.5}\text{Cu}_1\text{Nb}_3\text{Si}_{15.5}\text{B}_7$ alloy, according to the XRD analysis (**Figure 5**). However, it can be observed that the average crystallite size of α -Fe(Si)

phase in the $\text{Fe}_{73,5}\text{Cu}_1\text{Nb}_3\text{Si}_{15,5}\text{B}_7$ alloy remains the same, around 15 nm, over a wide temperature range. This is expected as a consequence of the presence of Nb atoms in the amorphous matrix, which, due to their large atomic radius, hinder the diffusion of Fe and Si to the crystal, obstructing its further growth [14]. When crystallization of the phase containing Nb starts, further crystal growth of $\alpha\text{-Fe}(\text{Si})$ phase occurs.

For all the alloys examined, the average crystallite size of the $\alpha\text{-Fe}(\text{Si})$ phase at the highest temperatures amounts to 80–100 nm, except for the $\text{Fe}_{79,8}\text{Ni}_{1,5}\text{Si}_{5,2}\text{B}_{13}\text{C}_{0,5}$ alloy, where it is around 35 nm. This exception can originate from the crystallization kinetics of individual steps of formation of $\alpha\text{-Fe}(\text{Si})$ phase in this alloy, where a higher ratio of the nucleation rate to the crystal growth rate than in the other alloys examined occurs. On the other hand, when it comes to another phase observed in all the alloys containing Fe as the dominant component, Fe_2B , its crystallite size reaches approximately 50 nm after heating at the highest temperatures, except for the $\text{Fe}_{73,5}\text{Cu}_1\text{Nb}_3\text{Si}_{15,5}\text{B}_7$ alloy, where the size of around 30 nm is contributed by lower boron content in the alloy. In the case of the alloy containing 40 atomic % of iron, in accordance with the chemical composition and unique phase compositions, during thermal treatment, the average crystallite size of the formed phases changes slightly in temperature ranges in which nucleation is the dominant process or exhibits more pronounced changes in temperature intervals where the crystal growth dominates [18].

3.4 Influence of thermal treatment on functional properties

Functional properties of the as-prepared and thermally treated amorphous alloys are significantly influenced by their microstructure beside the chemical composition. In the case of very low thermal effects, thermally induced microstructural transformations are more noticeable in the changes of functional properties than by thermal analysis. Bearing this in mind as well as potential practical application of the studied alloys, microhardness, thermomagnetic resistivity, and electrical resistivity analyses were performed.

3.4.1 Microhardness

In the as-prepared form, the examined alloys exhibit relatively high microhardness values, over 900 HV [20, 26, 30], as shown for the $\text{Fe}_{73,5}\text{Cu}_1\text{Nb}_3\text{Si}_{15,5}\text{B}_7$, $\text{Fe}_{75}\text{Ni}_2\text{Si}_8\text{B}_{13}\text{C}_2$, and $\text{Fe}_{81}\text{B}_{13}\text{Si}_4\text{C}_2$ alloys (**Figure 6a**). Thermally induced formation of nanocrystalline structure results in an increase in the microhardness value, which reaches maximum at around 500–600°C and then declines (**Figure 6a**). The

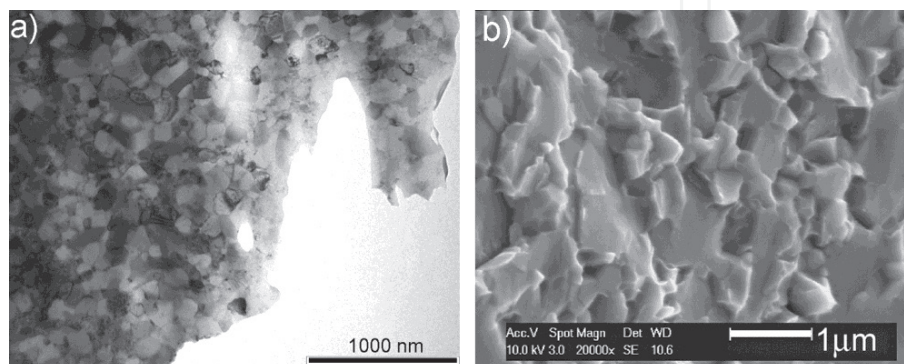


Figure 4. TEM image of the $\text{Fe}_{73,5}\text{Cu}_1\text{Nb}_3\text{Si}_{15,5}\text{B}_7$ alloy sample annealed at 725°C (a) and SEM image of the cross section of the $\text{Fe}_{73,5}\text{Cu}_1\text{Nb}_3\text{Si}_{15,5}\text{B}_7$ alloy sample annealed at 850°C for 24 h (b) as the examples showing the microstructure of the crystallized alloy.

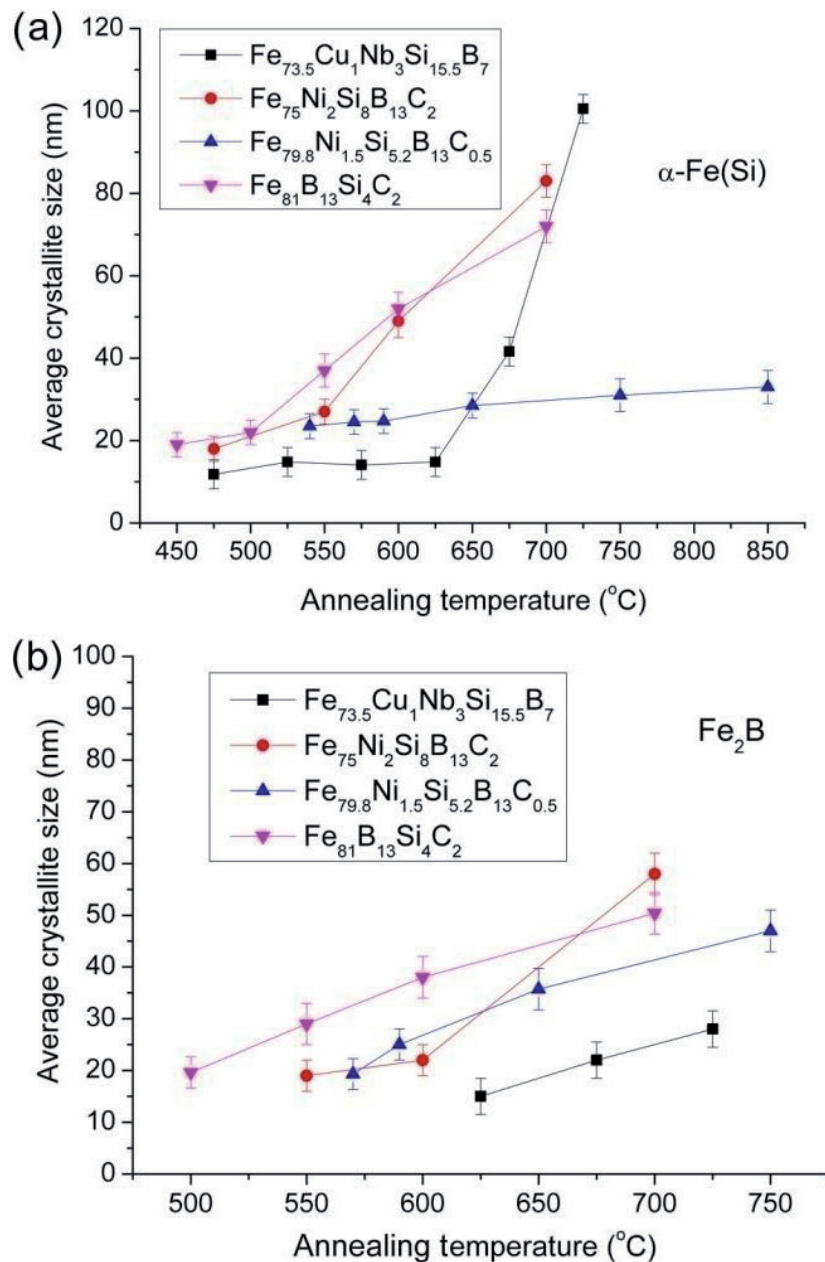


Figure 5. Average crystallite size of the α -Fe(Si) (a) and Fe₂B (b) phases in the alloys containing 73–81 atomic % of iron, after thermal treatment at different temperatures.

maximal microhardness values correspond to the optimal microstructure, consisting of a composite involving nanocrystals embedded in amorphous matrix. This structure has a lower interfacial energy than purely amorphous or purely crystalline structure with crystal/crystal interface, suppressing propagation of shear bands and cracks along the interfaces [20, 26, 30]. At higher temperatures of thermal treatment, the dominant crystal/crystal interface with higher interfacial energy leads to easier shear band and crack propagation, yielding lower microhardness values.

3.4.2 Thermomagnetic measurements

Thermomagnetic measurements on heating [18, 20, 25, 28] revealed thermally induced microstructural changes, influencing the magnetic properties of the alloys. All the studied alloys exhibit two Curie temperatures (**Figure 7**), one corresponding to the as-prepared alloy (T_{c1}) and the second one corresponding to the Curie temperature of the alloy in the crystallized form (T_{c2}) (**Table 1**). The alloys

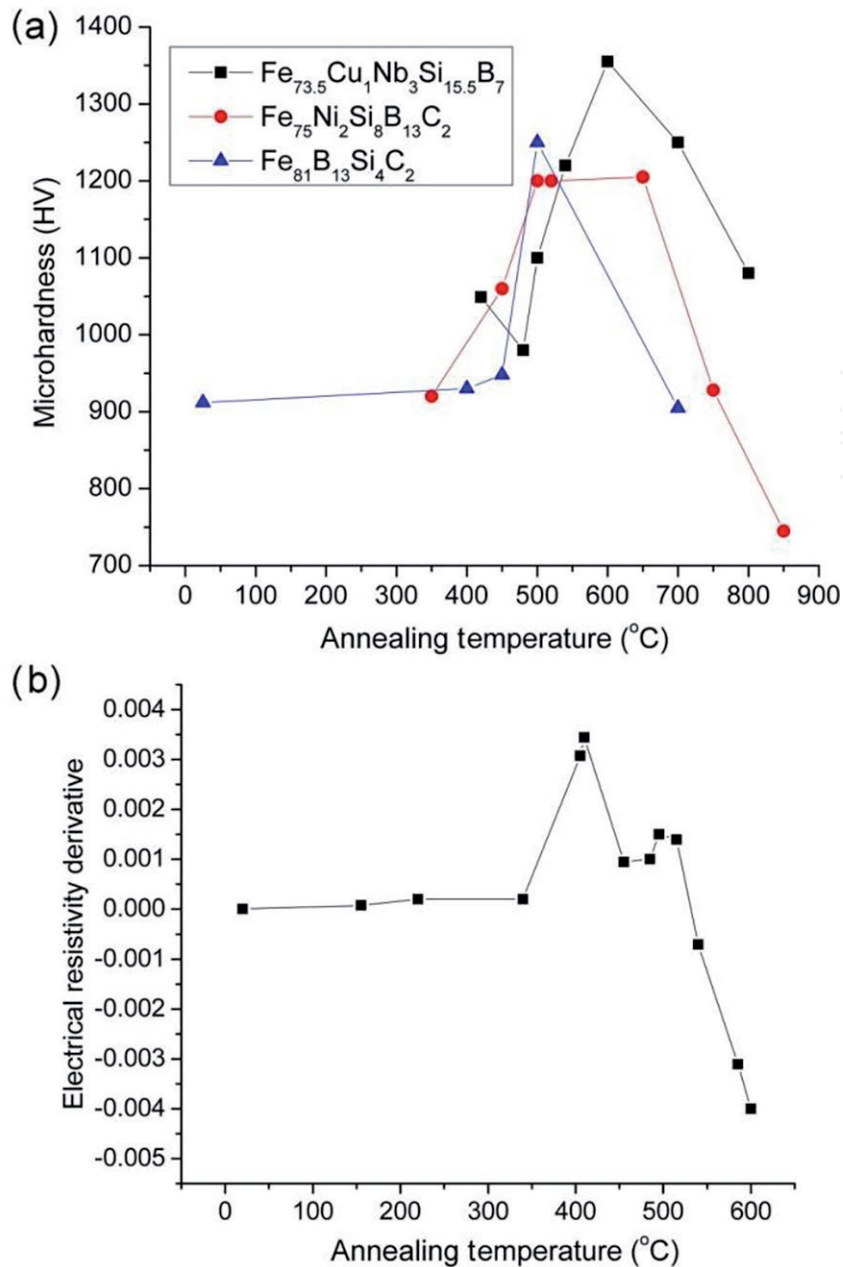


Figure 6.

Microhardness values of the $\text{Fe}_{73.5}\text{Cu}_1\text{Nb}_3\text{Si}_{15.5}\text{B}_7$, $\text{Fe}_{75}\text{Ni}_2\text{Si}_8\text{B}_{13}\text{C}_2$, and $\text{Fe}_{81}\text{B}_{13}\text{Si}_4\text{C}_2$ alloys after annealing at different temperatures (a) and the first derivative of the curve of temperature dependence of electrical resistivity for $\text{Fe}_{81}\text{B}_{13}\text{Si}_4\text{C}_2$ alloys (reprinted from ref. [29] with permission of Elsevier) (b).

$\text{Fe}_{75}\text{Ni}_2\text{Si}_8\text{B}_{13}\text{C}_2$ and $\text{Fe}_{81}\text{B}_{13}\text{Si}_4\text{C}_2$ exhibit similar values of the first Curie temperature, as a result of similarities in their chemical composition including high Fe content, and equal percentages of B and C. The lowest values of the first Curie temperature are observed for the $\text{Fe}_{73.5}\text{Cu}_1\text{Nb}_3\text{Si}_{15.5}\text{B}_7$ and $\text{Fe}_{40}\text{Ni}_{40}\text{P}_{14}\text{B}_6$ alloys. In the case of $\text{Fe}_{73.5}\text{Cu}_1\text{Nb}_3\text{Si}_{15.5}\text{B}_7$ alloy, low value of the first Curie temperature is provoked by the presence of Nb. It is well known that the addition of Nb reduces the Curie temperature of the amorphous phase by around 25% per atomic percent of Nb, while the influence of Cu is negligible [39]. Relatively low Fe content, relatively high Ni content, and the presence of P in the amorphous $\text{Fe}_{40}\text{Ni}_{40}\text{P}_{14}\text{B}_6$ alloy result in low value of the Curie temperature of this alloy. This is a consequence of the facts that Ni has lower Curie temperature and lower magnetic moment than Fe and the P addition has a decreasing effect on magnetic moment [40].

The beginning of crystallization process (Figure 7), as a result of formation of various magnetic crystalline phases, leads to an increase in magnetic moment of polycrystalline alloys. The manner of magnetic moment growth during the

crystallization and subsequent decline when approaching the T_{c2} are determined by phase compositions of individual crystallized alloys. Thus, for example, in the case of $\text{Fe}_{73.5}\text{Cu}_1\text{Nb}_3\text{Si}_{15.5}\text{B}_7$, a rise in magnetic moment can be observed up to around 550°C , and then its drop starts, moving toward the Curie temperature of the formed crystalline phases. It should be noted that for the FINEMET-type alloys, to which $\text{Fe}_{73.5}\text{Cu}_1\text{Nb}_3\text{Si}_{15.5}\text{B}_7$ belongs, literature data [3, 41] usually include only the second value of Curie temperature because of its importance for practical application, since these alloys are mostly used in nanocrystalline form obtained by partial crystallization of amorphous precursor. Similarity of the T_{c2} values of the $\text{Fe}_{75}\text{Ni}_2\text{Si}_8\text{B}_{13}\text{C}_2$ and $\text{Fe}_{81}\text{B}_{13}\text{Si}_4\text{C}_2$ alloys results from their very similar phase composition in the fully crystalline form. However, the lowest T_{c2} value was observed for the $\text{Fe}_{40}\text{Ni}_{40}\text{P}_{14}\text{B}_6$ alloy, because the phases γ -(Fe,Ni) and $(\text{Fe,Ni})_3(\text{P,B})$ which constitute fully crystalline alloy are characterized by lower Curie temperature values than the α -Fe(Si) and Fe_2B phases forming the alloys with Fe as the dominant component.

3.4.3 Electrical resistivity measurements

Electrical resistivity measurements performed on the alloys containing 73–81 atomic % of iron [15, 27, 29, 42], at room temperature, reveal that the as-prepared $\text{Fe}_{79.8}\text{Ni}_{1.5}\text{Si}_{5.2}\text{B}_{13}\text{C}_{0.5}$ and $\text{Fe}_{81}\text{B}_{13}\text{Si}_4\text{C}_2$ alloys exhibit slightly lower electrical resistivity values, and better electronic conductivity, than the $\text{Fe}_{73.5}\text{Cu}_1\text{Nb}_3\text{Si}_{15.5}\text{B}_7$ and $\text{Fe}_{75}\text{Ni}_2\text{Si}_8\text{B}_{13}\text{C}_2$ alloys (**Table 3**), which is attributed to their somewhat higher iron content. As expected, after heating at different temperatures, each structural transformation is followed by certain changes in the trend of temperature dependence of electrical resistivity [15, 27, 29, 42].

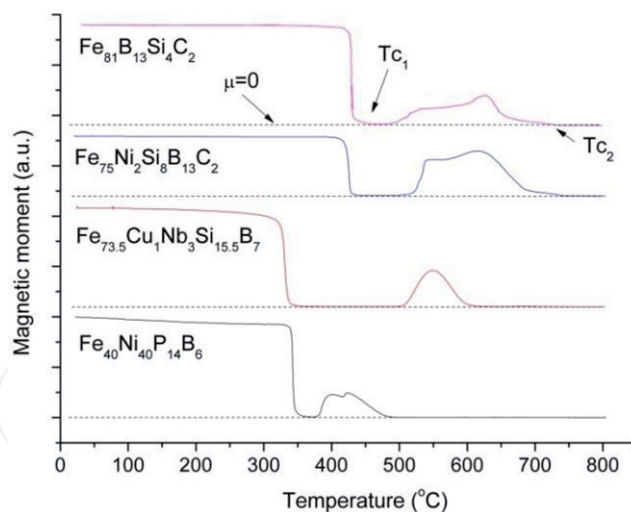


Figure 7.
 Thermomagnetic curves recorded at $4^\circ\text{C}/\text{min}$.

Alloy	Electrical resistivity ($\mu\Omega\text{m}$)
$\text{Fe}_{81}\text{B}_{13}\text{Si}_4\text{C}_2$	1.71
$\text{Fe}_{79.8}\text{Ni}_{1.5}\text{Si}_{5.2}\text{B}_{13}\text{C}_{0.5}$	1.73
$\text{Fe}_{75}\text{Ni}_2\text{Si}_8\text{B}_{13}\text{C}_2$	2.27
$\text{Fe}_{73.5}\text{Cu}_1\text{Nb}_3\text{Si}_{15.5}\text{B}_7$	2.13

Table 3.
 Electrical resistivity of the as-prepared alloys containing 73–81 atomic % of iron at room temperature.

The influence of thermally induced structural transformations on electrical resistivity of amorphous alloy can be illustrated with the example of $\text{Fe}_{75}\text{Ni}_2\text{Si}_8\text{B}_{13}\text{C}_2$ alloys [27]. In the temperature range 20–500°C, thermal treatment causes an increase in electrical resistivity (**Table 4**), where the slightly faster growth in the region 250–400°C corresponds to the structural relaxation, while the sharp increase occurs near the Curie point (400–430°C) [27]. Crystallization process, which starts at around 500°C, involves the sudden decline in electrical resistivity, since the ordered structure possesses lower electrical resistivity than the amorphous one. The second heating of the crystallized alloy results in linear growth of electrical resistivity with temperature [27], which is typical behavior of electronic (metal) conductors.

Measurement of electrical resistivity of the $\text{Fe}_{81}\text{B}_{13}\text{Si}_4\text{C}_2$ alloy after thermal treatment represents a good example of the situation when the functional properties are more sensitive to microstructural changes than thermal analysis. Derivative curve of the temperature dependence of electrical resistivity exhibits two well-defined maxima in the crystallization region (**Figure 6b**) [29], indicating that the crystallization in this case is a multistep process, although it occurs as a single peak in the DSC curve.

3.5 Crystallization kinetics

The knowledge of crystallization kinetics, besides thermal stability, is very important for usage of these alloys in modern technology, in order to estimate their applicability. The increase in heating rate leads to a shift in DSC peak temperature toward the region of higher temperatures [19, 21–24], showing that the observed processes are thermally activated, allowing the application of Arrhenius equation for kinetic description of the examined processes.

The kinetics of single-step solid-state phase transformation can be described using the equation:

$$\beta \frac{d\alpha}{dT} = A \exp\left(\frac{-E_a}{RT}\right) f(\alpha) \quad (1)$$

where T is the temperature, R is the gas constant, α is the conversion degree, β is the heating rate, $f(\alpha)$ is the conversion function representing the kinetic model, E_a is the activation energy, and A is the pre-exponential factor. The two last mentioned parameters are Arrhenius parameters, while the set including E_a , A and $f(\alpha)$ represents the kinetic triplet. For full kinetic description of a process, determination of kinetic triplet is required. Practical significance of kinetic triplets is determination of material lifetimes related to structural stability of materials and process rates [43].

Most of the observed crystallization DSC peaks are asymmetric as a result of complexity of crystallization processes involving more than one crystallization step. In order to study the kinetics of individual steps, complex crystallization peak deconvolution by application of appropriate mathematical procedure [19, 21–24] is required. For confirmation of single-step processes, isoconversional methods [43–49] are used.

Crystallization apparent activation energies for the formation of individual phases in the examined amorphous alloys, determined using Kissinger method [44], are presented in **Table 5**. The values obtained for the α -Fe(Si) phase are in the range 300–400 kJ/mol, while 200–350 kJ/mol are those determined for the Fe_2B phase. For all the crystalline phases in all the alloys examined, relatively high E_a values are obtained, probably as a result of cooperative participation of a large number of atoms in each step of the transformations [36]. The E_a values, obtained

Temperature (°C)	Electrical resistivity ($\mu\Omega\text{m}$)
20	2.268
100	2.282
150	2.296
200	2.310
250	2.331
350	2.408
400	2.492
410	2.548
440	2.576
530	2.604
540	2.604
545	2.492
550	2.352

Table 4. Electrical resistivity measurements performed on the $\text{Fe}_{75}\text{Ni}_2\text{Si}_8\text{B}_{13}\text{C}_2$ alloy after thermal treatment at different temperatures.

using various methods [19, 21–24], are in agreement with the literature overall E_a values corresponding to the similar systems [36, 50, 51].

The alloys containing 73–81 atomic % of Fe, except the $\text{Fe}_{81}\text{B}_{13}\text{Si}_4\text{C}_2$, have lower crystallization apparent activation energy for the Fe_2B phase than that of the $\alpha\text{-Fe}(\text{Si})$ phase by approximately 25%. This is a consequence of the creation of favorable conditions for crystallization of Fe_2B phase by enrichment of amorphous matrix with B caused by crystallization of $\alpha\text{-Fe}(\text{Si})$ grains. The similar values of apparent activation energy of crystallization for the $\alpha\text{-Fe}(\text{Si})$ and Fe_2B phases in the $\text{Fe}_{81}\text{B}_{13}\text{Si}_4\text{C}_2$ alloy can be explained by the presence of crystalline phase in amount of around 5% in the as-prepared structure acting as crystallization seeds and facilitating the crystallization of the $\alpha\text{-Fe}(\text{Si})$ phase from the amorphous matrix. Higher value of apparent activation energy of crystallization of $\alpha\text{-Fe}(\text{Si})$ can be observed for the $\text{Fe}_{79.8}\text{Ni}_{1.5}\text{Si}_{5.2}\text{B}_{13}\text{C}_{0.5}$ alloy due to the high thermal stability of this alloy, which originates from its optimal chemical composition. In the case of the alloy with high Ni content, formation of the bcc structure entails somewhat higher apparent activation energy (Table 5).

Kinetic analysis [19, 21–24] reveals that the conditions for application of the JMA model, most commonly used for kinetic description of transformations that consisted of nucleation and crystal growth processes, are not entirely fulfilled for any crystallization step in the alloys examined. Actually, for all crystallization steps, the shape of the Málek's curves [52] corresponds to the JMA model, but the maxima of the $z(\alpha)$ functions are shifted toward lower α values. Nucleation, which does not occur only in the early stages of transformations, and hard impingement effects corresponding to anisotropic crystal growth are the main contributors to such behavior. Anisotropic crystal growth is also indicated by the appearance of preferential orientation, observed during microstructural analysis [17]. Considering good accordance among the Málek's curves obtained at different heating rates, it can be concluded that the mechanism of the studied process does not change with heating rate in the range of heating rates examined. Autocatalytic Šesták-Berggren model, in two-parameter form $f(\alpha) = \alpha^M(1 - \alpha)^N$,

best describes the kinetics of crystallization, for all crystallization steps [19, 21–24]. Conversion functions of individual crystallization steps, in different alloys, are presented in **Table 5**. By introducing the kinetic triplets of individual crystallization steps into the equation for the solid-state transformation rate, with corresponding normalization and summation, simulated DSC curves can be obtained, which are, for the studied processes, in full accordance with experimental DSC curves [19, 21, 23], confirming the validity of the obtained kinetic triplets (**Figure 8**).

More information on crystallization mechanism can be obtained by considering values of local Avrami exponent, n [53]. Local Avrami exponent as well as the manner of its change with the progress of the process can indicate a certain transformation mechanism. For all crystallization steps of the examined alloys, decline in n value with the progress of transformation is observed (**Figure 9**) [19, 21]. This suggests the occurrence of impingement during the crystal growth, which was also indicated by microstructural analysis, as mentioned previously [19–21]. For non-isothermal measurements, at constant heating rates, conversion degree which corresponds to the position of the transformation rate maximum (α_p) suggests the anisotropic crystal growth as the prevailing type of impingement [54]. This includes blocking effects of growing particles occurring earlier than those for the isotropic growth, leading to hard impingement and to deviation from the classical JMA model [54]. Anisotropic crystal growth was also suggested by the existence of preferential orientation [17].

After determining the kinetic triplets, the lifetime of the alloys against crystallization which reflects their thermal stability as well as the stability of their functional properties is estimated. For the conversion degree of 5%, at room temperature, the alloys exhibit high lifetime values (10^{27} – 10^{39} years) (**Table 6**), indicating that these materials are very stable at room temperature, in spite of their thermodynamic and kinetic metastability [21, 23]. Nevertheless, an increase in the

Phase	Alloy	E_a (kJ mol ⁻¹)	lnA (A/min ⁻¹)	$f(\alpha)$
α -Fe(Si)	Fe ₈₁ B ₁₃ Si ₄ C ₂	320 ± 10	48 ± 2	$\alpha^{0.69}(1-\alpha)^{0.99}$
	Fe _{79.8} Ni _{1.5} Si _{5.2} B ₁₃ C _{0.5}	399 ± 6	58 ± 2	$\alpha^{0.98}(1-\alpha)^{1.20}$
	Fe ₇₅ Ni ₂ Si ₈ B ₁₃ C ₂	298 ± 7	44 ± 1	$\alpha^{0.51}(1-\alpha)^{1.16}$
	Fe _{73.5} Cu ₁ Nb ₃ Si _{15.5} B ₇	335 ± 7	49 ± 1	$\alpha^{0.46}(1-\alpha)^{1.20}$
Fe ₃ B	Fe ₈₁ B ₁₃ Si ₄ C ₂	332 ± 5	50 ± 1	$\alpha^{0.69}(1-\alpha)^{0.93}$
	Fe ₇₅ Ni ₂ Si ₈ B ₁₃ C ₂	230 ± 10	33 ± 3	$\alpha^{0.64}(1-\alpha)$
Fe ₂ B	Fe ₈₁ B ₁₃ Si ₄ C ₂	340 ± 20	50 ± 3	$\alpha^{0.78}(1-\alpha)^{0.92}$
	Fe _{79.8} Ni _{1.5} Si _{5.2} B ₁₃ C _{0.5}	300 ± 10	43 ± 2	$\alpha(1-\alpha)^{1.30}$
	Fe ₇₅ Ni ₂ Si ₈ B ₁₃ C ₂	210 ± 20	29 ± 4	$\alpha^{0.62}(1-\alpha)$
	Fe _{73.5} Cu ₁ Nb ₃ Si _{15.5} B ₇	260 ± 20	37 ± 3	$\alpha^{0.51}(1-\alpha)^{1.30}$
Fe ₁₆ Nb ₆ Si ₇	Fe _{73.5} Cu ₁ Nb ₃ Si _{15.5} B ₇	490 ± 10	60 ± 2	$\alpha(1-\alpha)^{1.40}$
Fe ₂ Si	Fe _{73.5} Cu ₁ Nb ₃ Si _{15.5} B ₇	470 ± 30	58 ± 5	$\alpha^{0.60}(1-\alpha)^{1.10}$
α -(Fe,Ni)	Fe ₄₀ Ni ₄₀ P ₁₄ B ₆	450 ± 20	82 ± 3	$\alpha^{0.53}(1-\alpha)^{1.11}$
γ -(Fe,Ni)	Fe ₄₀ Ni ₄₀ P ₁₄ B ₆	450 ± 30	80 ± 5	$\alpha^{0.50}(1-\alpha)^{1.15}$
(Fe,Ni) ₃ (P,B)	Fe ₄₀ Ni ₄₀ P ₁₄ B ₆	460 ± 30	81 ± 6	$\alpha^{0.48}(1-\alpha)^{1.18}$

Table 5.
Kinetic triplets of individual crystallization steps determined for different alloys.

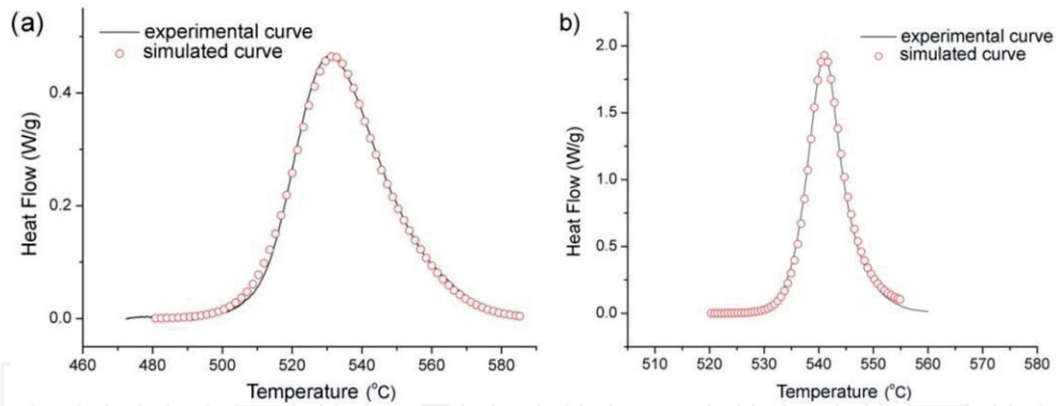


Figure 8. Examples of comparison of experimental DSC curves at 8°C/min and the curves simulated with determined kinetic triplets of individual crystallization steps: $\text{Fe}_{73.5}\text{Cu}_1\text{Nb}_3\text{Si}_{15.5}\text{B}_7$ alloy, peak 1 (a), and $\text{Fe}_{79.8}\text{Ni}_{1.5}\text{Si}_{5.2}\text{B}_{13}\text{C}_{0.5}$ alloy (b).

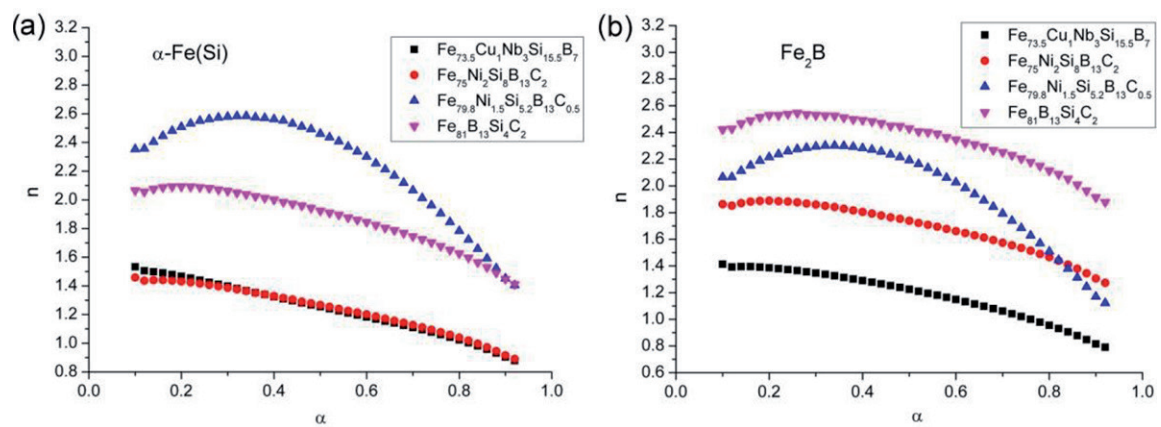


Figure 9. Local values of Avrami exponent of $\alpha\text{-Fe(Si)}$ (a) and Fe_2B (b) phases in different alloys at 5°C/min.

Alloy	Lifetime (year)
$\text{Fe}_{81}\text{B}_{13}\text{Si}_4\text{C}_2$	2.2×10^{29}
$\text{Fe}_{79.8}\text{Ni}_{1.5}\text{Si}_{5.2}\text{B}_{13}\text{C}_{0.5}$	3.6×10^{39}
$\text{Fe}_{75}\text{Ni}_2\text{Si}_8\text{B}_{13}\text{C}_2$	2.5×10^{27}
$\text{Fe}_{73.5}\text{Cu}_1\text{Nb}_3\text{Si}_{15.5}\text{B}_7$	2.2×10^{30}
$\text{Fe}_{40}\text{Ni}_{40}\text{P}_{14}\text{B}_6$	3.3×10^{38}

Table 6. Estimated values of the lifetime of the alloys against crystallization at room temperature, determined for conversion degree of 5%.

temperature of thermal treatment leads to an exponential decline in the values of estimated lifetime against crystallization, which amounts to only several minutes at the temperature of the onset of crystallization process [21, 23]. At room temperature, the amorphous $\text{Fe}_{79.8}\text{Ni}_{1.5}\text{Si}_{5.2}\text{B}_{13}\text{C}_{0.5}$ alloy shows lifetime value by several orders of magnitude higher than those of the other alloys containing 73–81 atomic % of Fe, which is in accordance with its higher thermal stability. In spite of crystallizing at lower temperatures than the alloys with 73–81 atomic % of Fe, the alloy containing 40 atomic % of Fe shows higher thermal stability at room temperature, manifested by higher lifetime values than those of the alloys containing Fe as the dominant component (Table 6).

4. Conclusion

A detailed study of five iron-based amorphous alloys with the compositions $\text{Fe}_{81}\text{Si}_4\text{B}_{13}\text{C}_2$, $\text{Fe}_{79.8}\text{Ni}_{1.5}\text{Si}_{5.2}\text{B}_{13}\text{C}_{0.5}$, $\text{Fe}_{75}\text{Ni}_2\text{Si}_8\text{B}_{13}\text{C}_2$, $\text{Fe}_{73.5}\text{Cu}_1\text{Nb}_3\text{Si}_{15.5}\text{B}_7$, and $\text{Fe}_{40}\text{Ni}_{40}\text{P}_{14}\text{B}_6$ revealed that the alloy behavior in terms of mechanism, thermodynamics, and kinetics of thermally induced microstructural transformations, as well as the functional properties, is significantly influenced by chemical composition of the alloy. The highest thermal stability among the studied alloys was observed for the $\text{Fe}_{79.8}\text{Ni}_{1.5}\text{Si}_{5.2}\text{B}_{13}\text{C}_{0.5}$ alloy due to its optimal chemical composition. Crystallization changed alloy microstructure and morphology, making the alloys grainy and more porous, influencing the functional properties of the alloys. Crystalline $\alpha\text{-Fe}(\text{Si})$ and Fe_2B phases were observed to be the final crystallization products in all the alloys with Fe as the dominant component. Kinetic analysis of individual crystallization steps, performed after peak deconvolution, revealed around 25% lower apparent activation energy values of the Fe_2B phase than those of the $\alpha\text{-Fe}(\text{Si})$ phase, for most of the studied alloys, as a result of promoted Fe_2B crystallization by formation of $\alpha\text{-Fe}(\text{Si})$ grains and an enrichment of the amorphous matrix with boron. Relatively high stability of the studied alloys against crystallization was observed at room temperature in spite of thermodynamic metastability and kinetic metastability of amorphous materials, with its abrupt drop at increased temperatures.

Acknowledgements

This research was supported by the Ministry of Education, Science and Technological Development of the Republic of Serbia, under the Project No. OI172015.

Author details

Milica M. Vasić¹, Dušan M. Minić² and Dragica M. Minić^{1*}

¹ Faculty of Physical Chemistry, University of Belgrade, Belgrade, Serbia

² Military Technical Institute, Belgrade, Serbia

*Address all correspondence to: dminic@ffh.bg.ac.rs

IntechOpen

© 2019 The Author(s). Licensee IntechOpen. This chapter is distributed under the terms of the Creative Commons Attribution License (<http://creativecommons.org/licenses/by/3.0>), which permits unrestricted use, distribution, and reproduction in any medium, provided the original work is properly cited. 

References

- [1] Takayama S. Amorphous structures and their formation and stability. *Journal of Materials Science*. 1976;**11**:164-185
- [2] Flohrer S, Herzer G. Random and uniform anisotropy in soft magnetic nanocrystalline alloys. *Journal of Magnetism and Magnetic Materials*. 2010;**322**:1511-1514
- [3] Suryanarayana C, Inoue A. Iron-based bulk metallic glasses. *International Materials Review*. 2013;**58**:131-166
- [4] Shen B, Inoue A. Superhigh strength and good soft-magnetic properties of (Fe,Co)-B-Si-Nb bulk glassy alloys with high glass-forming ability. *Applied Physics Letters*. 2004;**85**:4911-4913
- [5] Pang S, Zhang T, Asami K, Inoue A. Effects of chromium on the glass formation and corrosion behavior of bulk glassy Fe-Cr-Mo-C-B alloys. *Materials Transactions*. 2002;**43**:2137-2142
- [6] Gavrilović A, Rafailović LD, Minić DM, Wosik J, Angerer P, Minić DM. Influence of thermal treatment on structure development and mechanical properties of amorphous $\text{Fe}_{73.5}\text{Cu}_1\text{Nb}_3\text{Si}_{15.5}\text{B}_7$ ribbon. *Journal of Alloys and Compounds*. 2011;**509S**:S119-S122
- [7] McHenry ME, Willard MA, Laughlin DE. Amorphous and nanocrystalline materials for applications as soft magnets. *Progress in Materials Science*. 1999;**44**:291-433
- [8] Gu XJ, Poon SJ. Mechanical properties of iron-based bulk metallic glasses. *Journal of Materials Research*. 2007;**22**:344-351
- [9] Inoue A, Shen B. Formation and soft magnetic properties of Fe-B-Si-Zr bulk glassy alloys with high saturation magnetization above 1.5 T. *Materials Transactions*. 2002;**43**:2350-2353
- [10] Inoue A. High strength bulk amorphous alloys with low critical cooling rates. *Materials Transactions*. 1995;**36**:866-875
- [11] Greer AL. Confusion by design. *Nature*. 1993;**366**:303-304
- [12] Du SW, Ramanujan RV. Crystallization and magnetic properties of $\text{Fe}_{40}\text{Ni}_{38}\text{B}_{18}\text{Mo}_4$ amorphous alloy. *Journal of Non-Crystalline Solids*. 2005;**351**:3105-3113
- [13] Gleiter H. Nanocrystalline materials. *Progress in Materials Science*. 1989;**33**:223-315
- [14] Kulik T. Nanocrystallization of metallic glasses. *Journal of Non-Crystalline Solids*. 2001;**287**:145-161
- [15] Blagojević VA, Minić DM, Vasić M, Minić DM. Thermally induced structural transformations and their effect on functional properties of $\text{Fe}_{89.8}\text{Ni}_{1.5}\text{Si}_{5.2}\text{B}_3\text{C}_{0.5}$ amorphous alloy. *Materials Chemistry and Physics*. 2013;**142**:207-212
- [16] Vasić MM, Minić DM, Blagojević VA, Žák T, Pizúrová N, David B, et al. Thermal stability and mechanism of thermally induced crystallization of $\text{Fe}_{73.5}\text{Cu}_1\text{Nb}_3\text{Si}_{15.5}\text{B}_7$ amorphous alloy. *Acta Physica Polonica, A*. 2015;**128**:657-660
- [17] Blagojević VA, Vasić M, David B, Minić DM, Pizúrová N, Žák T, et al. Thermally induced crystallization of $\text{Fe}_{73.5}\text{Cu}_1\text{Nb}_3\text{Si}_{15.5}\text{B}_7$ amorphous alloy. *Intermetallics*. 2014;**45**:53-59
- [18] Vasić MM, Roupcová P, Pizúrová N, Stevanović S, Blagojević VA, Žák T, et al. Thermally induced structural

- transformations of $\text{Fe}_{40}\text{Ni}_{40}\text{P}_{14}\text{B}_6$ amorphous alloy. *Metallurgical and Materials Transactions A*. 2016;**47A**:260-267
- [19] Vasić MM, Blagojević VA, Begović NN, Žák T, Pavlović VB, Minić DM. Thermally induced crystallization of amorphous $\text{Fe}_{40}\text{Ni}_{40}\text{P}_{14}\text{B}_6$ alloy. *Thermochimica Acta*. 2015;**614**:129-136
- [20] Blagojević VA, Vasić MM, David B, Minić DM, Pizúrová N, Žák T, et al. Microstructure and functional properties of $\text{Fe}_{73.5}\text{Cu}_1\text{Nb}_3\text{Si}_{15.5}\text{B}_7$ amorphous alloy. *Materials Chemistry and Physics*. 2014;**145**:12-17
- [21] Vasić MM, Minić DM, Blagojević VA, Minić DM. Kinetics and mechanism of thermally induced crystallization of amorphous $\text{Fe}_{73.5}\text{Cu}_1\text{Nb}_3\text{Si}_{15.5}\text{B}_7$ alloy. *Thermochimica Acta*. 2014;**584**:1-7
- [22] Blagojević VA, Vasić M, Minić DM, Minić DM. Kinetics and thermodynamics of thermally induced structural transformations of amorphous $\text{Fe}_{75}\text{Ni}_2\text{Si}_8\text{B}_{13}\text{C}_2$ alloy. *Thermochimica Acta*. 2012;**549**:35-41
- [23] Vasić M, Minić DM, Blagojević VA, Minić DM. Mechanism and kinetics of crystallization of amorphous $\text{Fe}_{81}\text{B}_{13}\text{Si}_4\text{C}_2$ alloy. *Thermochimica Acta*. 2013;**572**:45-50
- [24] Vasić M, Minić DM, Blagojević VA, Minić DM. Mechanism of thermal stabilization of $\text{Fe}_{89.8}\text{Ni}_{1.5}\text{Si}_{5.2}\text{B}_3\text{C}_{0.5}$ amorphous alloy. *Thermochimica Acta*. 2013;**562**:35-41
- [25] Minić DM, Blagojević VA, Maričić AM, Žák T, Minić DM. Influence of structural transformations on functional properties of $\text{Fe}_{75}\text{Ni}_2\text{Si}_8\text{B}_{13}\text{C}_2$ amorphous alloy. *Materials Chemistry and Physics*. 2012;**134**:111-115
- [26] Blagojević VA, Minić DM, Žák T, Minić DM. Influence of thermal treatment on structure and microhardness of $\text{Fe}_{75}\text{Ni}_2\text{Si}_8\text{B}_{13}\text{C}_2$ amorphous alloy. *Intermetallics*. 2011;**19**:1780-1785
- [27] Minić DM, Maričić AM. Influence of heating on electric and magnetic properties of $\text{Fe}_{75}\text{Ni}_2\text{B}_{13}\text{Si}_8\text{C}_2$ amorphous alloy. *Materials Science and Engineering B*. 2010;**172**:127-131
- [28] Minić DM, Minić DM, Žák T, Roupčová P, David B. Structural transformations of $\text{Fe}_{81}\text{B}_{13}\text{Si}_4\text{C}_2$ amorphous alloy induced by heating. *Journal of Magnetism and Magnetic Materials*. 2011;**323**:400-404
- [29] Minić DM, Minić DG, Maričić A. Stability and crystallization of $\text{Fe}_{81}\text{B}_{13}\text{Si}_4\text{C}_2$ amorphous alloy. *Journal of Non-Crystalline Solids*. 2009;**355**:2503-2507
- [30] Minić DM, Blagojević VA, Minić DM, Gavrilović A, Rafailović L, Žák T. Influence of microstructure on microhardness of $\text{Fe}_{81}\text{Si}_4\text{B}_{13}\text{C}_2$ amorphous alloy after thermal treatment. *Metallurgical and Materials Transactions A*. 2011;**42A**:4106-4112
- [31] *Inorganic Crystals Structure Database (ICSD)*. Eggenstein-Leopoldshafen, Germany: FIZ Karlsruhe; 2014
- [32] *JCPDS PDF-2 Database*. Newton Square, PA, USA: ICDD; 2005
- [33] *Crystallography Open Database*. Available from: <http://www.crystallography.net> [Accessed: September 1, 2014, June 15, 2016]
- [34] Lutterotti L. Total pattern fitting for the combined size-strain-stress-texture determination in thin film diffraction. *Nuclear Instruments and Methods in Physics Research-Section B*. 2010;**268**:334-340

- [35] Scherrer P. Göttinger Nachrichten. Journal of Mathematical Physics. 1918;**2**:98-100
- [36] Kaloshkin SD, Tomilin IA. The crystallization kinetics of amorphous alloys. *Thermochimica Acta*. 1996;**280/281**:303-317
- [37] Qin J, Gu T, Yang L, Bian X. Study on the structural relationship between the liquid and amorphous $\text{Fe}_{78}\text{Si}_9\text{B}_{13}$ alloys by ab initio molecular dynamics simulation. *Applied Physics Letters*. 2007;**90**:201909
- [38] Ma H, Wang W, Zhang J, Li G, Cao C, Zhang H. Crystallization and corrosion resistance of $(\text{Fe}_{0.78}\text{Si}_{0.09}\text{B}_{0.13})_{100-x}\text{Ni}_x$ ($x=0, 2$ and 5) glassy alloys. *Journal of Materials Science and Technology*. 2011;**27**:1169-1177
- [39] Miguel C, Kaloshkin S, Gonzalez J, Zhukov A. Curie temperature behaviour on annealing of Finemet type amorphous alloys. *Journal of Non-Crystalline Solids*. 2003;**329**:63-66
- [40] Becker JJ, Luborsky FE, Walter JL. Magnetic moments and curie temperatures of $(\text{Fe}, \text{Ni})_{80}(\text{P}, \text{B})_{20}$ amorphous alloys. *IEEE Transactions on Magnetics*. 1977;**13**:988-991
- [41] Yoshizawa Y, Oguma S, Yamauchi K. New Fe-based soft magnetic alloys composed of ultrafine grain structure. *Journal of Applied Physics*. 1988;**64**:6044-6046
- [42] Maričić AM, Minić DM, Blagojević VA, Kalezić-Glišović A, Minić DM. Effect of structural transformations preceding crystallization on functional properties of $\text{Fe}_{73.5}\text{Cu}_1\text{Nb}_3\text{Si}_{15.5}\text{B}_7$ amorphous alloy. *Intermetallics*. 2012;**21**:45-49
- [43] Vyazovkin S, Burnham AK, Criado JM, Pérez-Maqueda LA, Popescu C, Sbirrazzuoli N. ICTAC kinetics committee recommendations for performing kinetic computations on thermal analysis data. *Thermochimica Acta*. 2011;**520**:1-19
- [44] Kissinger HE. Reaction kinetics in differential thermal analysis. *Analytical Chemistry*. 1957;**29**:1702-1706
- [45] Ortega A. A simple and precise linear integral method for isoconversional data. *Thermochimica Acta*. 2008;**474**:81-86
- [46] Ozawa T. A new method of analyzing thermogravimetric data. *Bulletin of the Chemical Society of Japan*. 1965;**38**:1881-1886
- [47] Flynn JH, Wall LA. A quick, direct method for the determination of activation energy from thermogravimetric data. *Journal of Polymer Science Part C: Polymer Letters*. 1966;**4**:323-328
- [48] Vyazovkin S. Modification of the integral isoconversional method to account for variation in the activation energy. *Journal of Computational Chemistry*. 2001;**22**:178-183
- [49] Vyazovkin S. Evaluation of activation energy of thermally stimulated solid-state reactions under arbitrary variation of temperature. *Journal of Computational Chemistry*. 1997;**18**:393-402
- [50] Wang Y, Xu K, Li Q. Comparative study of non-isothermal crystallization kinetics between $\text{Fe}_{80}\text{P}_{13}\text{C}_7$ bulk metallic glass and melt-spun glassy ribbon. *Journal of Alloys and Compounds*. 2012;**540**:6-15
- [51] Santos DS, Santos DR. Crystallization kinetics of Fe-B-Si metallic glasses. *Journal of Non-Crystalline Solids*. 2002;**304**:56-63
- [52] Málek J. Kinetic analysis of crystallization processes in amorphous

materials. *Thermochimica Acta*.
2000;355:239-253

[53] Blazquez JS, Conde CF, Conde A.
Non-isothermal approach to
isokinetic crystallization processes:
Application to the nanocrystallization
of HITPERM alloys. *Acta Materialia*.
2005;53:2305-2311

[54] Liu F, Song SJ, Sommer F,
Mittemeijer EJ. Evaluation of the
maximum transformation rate
for analyzing solid-state phase
transformation kinetics. *Acta
Materialia*. 2009;57:6176-6190

IntechOpen